

# Design and Optimization of Ring-pair Permanent Magnets for Portable Magnetic Resonance Imaging Systems

Yi-Yuan Cheng, Ming-Yang Su, Yi-Ding Huang, Wei Liu

**Abstract**—Portable Magnetic Resonance Imaging (MRI) systems have been commonly employed in medical centers to quickly provide imaging diagnosis and reliable support for the equipment. Recently, ring-pair permanent magnets have exhibited impressive features in contrast with conventional magnetic counterparts that make them convenient to integrate into portable MRI designs. In this study, the electromagnetic field within the three-dimensional ring-pair magnet was evaluated by using the finite element analysis-based ANSYS software. Initially, ring-pair magnets were divided into small magnets with various blocks. Sensitivity analysis was used to assess the structural parameters of the ring-pair magnets. Key structural parameters significantly influencing the magnetic field (MF) in the central imaging area were identified and refined through the particle swarm optimization method. The optimized design of ring-pair magnet models assists in providing a intense and homogeneous MF distribution in the central imaging area. Hence, our results can lay the groundwork for the advancement of ring-pair magnets for portable MRI systems.

**Index Terms**—Optimization, Sensitivity analysis, Ring-pair permanent magnet, Magnetic resonance imaging

## I. INTRODUCTION

With advancements in the medical science, portable and mobile Magnetic Resonance Imaging (MRI) systems have become increasingly popular as they can be easily deployed in many non-traditional and non-hospital settings, such as nursing homes, stadiums, intensive-care units, operating rooms, ambulances, and emergency rooms. The

Manuscript received March 25, 2024; revised January 24, 2025. This work was supported by the Natural Science Foundation of Henan Province in China (Grant No. 242300420439), the Scientific and Technological Project of Henan Province in China (Grant No. 222102310466 & No. 232102211047), the Key Scientific Research Project of Henan Province in China (Grant No. 23A416005), and the Cultivation Fund Project of National Natural Science Foundation of Nanyang Normal University (Grant No. 2022PY023).

Yi-Yuan Cheng is an associate professor of Intelligent Manufacturing and Electrical Engineering Department, Nanyang Normal University, Nanyang, 473061, China. (phone: 86-0377-63520108 ; e-mail: chengyy850@gmail.com).

Ming-Yang Su is a lecturer of Mapping and Environmental Engineering Department, Henan Polytechnic Institute, Nanyang, 473000, China. (e-mail: sumingyang@foxmail.com).

Yi-Ding Huang is an associate professor of Intelligent Manufacturing and Electrical Engineering Department, Nanyang Normal University, Nanyang, 473061, China. (e-mail: huangyiding123@163.com).

Wei Liu is a professor of Intelligent Manufacturing and Electrical Engineering Department, Nanyang Normal University, Nanyang 473061, China. (e-mail: lw3171796@163.com).

magnet of MRI produces a homogeneous static magnetic field (MF) in the central imaging area with the imaging quality directly influenced by the intensity and uniformity of this field [1-2]. The magnet, being the core component with the largest volume and weight, is also the most expensive part of the MRI system. Resistive and superconducting magnets, with their complex structures requiring extra electrical power and liquid helium [3-4], are unsuitable for portable MRI systems. Therefore, a permanent magnet can be considered the leading alternative for such systems due to its simplicity and open-structure design, making the system cost-effective for commercial deployment.

Three types of permanent magnets, namely, bipolar, Halbach, and ring-pair, have been typically used in portable MRI systems. The specific structures of these magnets are illustrated in Fig. 1. A bipolar magnet comprises two permanent magnetic poles with iron yokes of different shapes (H- or C-type), and an H-type bipolar magnet as shown in Fig. 1(a). The iron yoke primarily guided the magnet's internal MF; however, the yoke increases the weight and volume of the magnet. Few studies have used this magnet for imaging outdoor plants [5] and human elbows [6]. Nonetheless, the imaging area of the magnet is relatively small. A Halbach magnet contains an array of several small permanent magnets often forming a closed ring [7], as portrayed in Fig. 1(b). Since no iron yoke is present, the magnet is relatively light in weight, thereby making it attractive for desktop and head imaging applications [7-8]. However, the MF being oriented perpendicularly is one of the key drawbacks of Halbach magnets. Similarly, the general radio frequency (RF) component needs redesigning due to its incompatibility with the latest design of MRI systems in the market. In recent times, the ring-pair magnet proposed by Aubert [9-10] has been explored and utilized for portable MRI systems [11-13]. The ring-pair magnet is composed of two permanent magnet rings magnetized radially inward and outward, respectively. As exhibited in Fig. 1(c), the black arrows represent the direction of radial magnetization. The MF direction produced by the ring-pair magnet is consistent with that of a superconducting magnet; therefore, the general RF coil is compatible with the system utilization making ring-pair magnets appealing for MRI systems as compared to the other two types of magnets. Although ring-pair magnets are yet to be commercialized as very few studies have been reported in the literature, research is being conducted on ring-pair magnets that are currently in the exploratory stage. Further research on ring-pair magnets is expected to set the developmental direction for optimum designing of future

portable MRI systems. This study focuses on the ring-pair magnet employed within a portable MRI system for brain imaging analysis and a series of simulations have been undertaken to optimize and design the system efficiently.

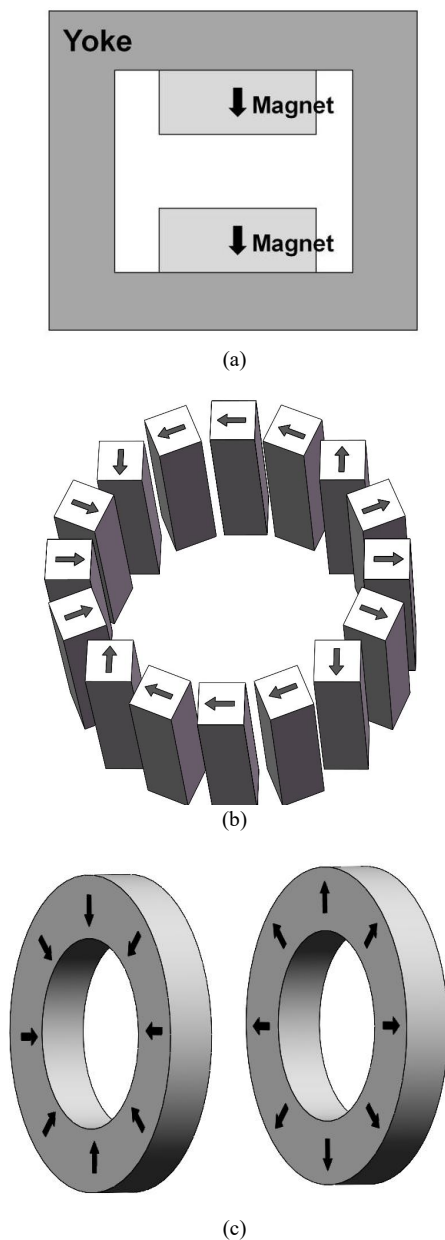


Fig. 1. Illustration of different magnets. (a) H-type bipolar magnet, (b) Halbach magnet(redrawing based on [7]), (c) Ring-pair magnet (redrawing based on [11]).

Designing and optimization of permanent magnets requires numerical techniques and relevant simulators for analyzing the electromagnetic field. Structural optimization of magnets is a time-consuming process that requires significant computing power to execute the designing process. Similarly, traditional optimization algorithms are unable to attain optimization solutions quickly in an effective manner. Therefore, in this work, a series of simulations have been performed on the ring-pair permanent magnet using the ANSYS software that utilizes the finite element analysis technique for calculating relevant parameters of the magnetic field. Furthermore, using global sensitivity analysis (SA), parametric studies were undertaken on a ring-pair permanent magnet to examine the impact of the related structural

parameters on magnetic field performance. These findings offer a foundation for refining the optimization process. Precise identification of key structural parameters influencing the magnetic field in the central imaging area prompts a reduction in the optimization problem size as well as curtailing the computational complexity issues. Finally, the particle swarm optimization (PSO) method was utilized to optimize the key structural parameters. The results indicate that the optimized ring-pair magnet models provide a uniform and strong MF distribution in the central imaging area.

## II. MODEL

A model of the ring-pair magnet designed for portable and mobile MRI systems is shown in Fig. 2. This magnet comprises two permanent magnet rings that are radially magnetized inward and outward, respectively. The black solid arrows in Fig. 2 represent the magnetization directions. The inner diameter  $R_{in}$  and the outer diameter  $R_{out}$  are 0.2 m and 0.4 m, respectively; the height  $H$  and the distance  $D$  between the two magnet rings are 0.1 m and 0.4 m, respectively. The central imaging field of view (FOV) is in the middle of the two permanent magnets. The FOV is considered as a cylinder with the diameter and height of 0.2 m and 0.05 m, respectively. Table I enlists all variables information of the model.

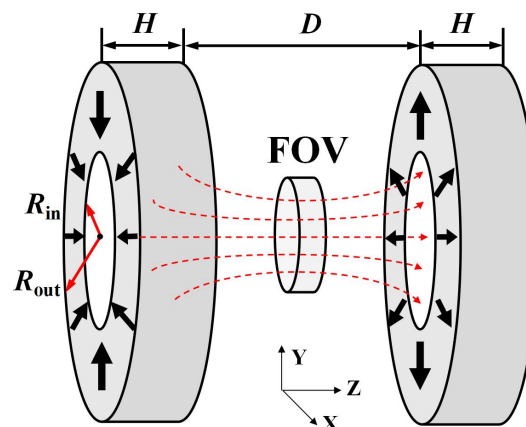


Fig. 2. Model of the ring-pair magnet.

TABLE I  
VARIABLES INFORMATION OF THE MODEL

Type	Description	Symbol	Value	Unit
Magnet Variable	Inner diameter	$R_{in}$	0.2	m
	Outer diameter	$R_{out}$	0.4	m
	Height of magnet ring	$H$	0.1	m
	Distance between two magnet rings	$D$	0.4	m
FOV variable	Diameter of cylinder	-	0.2	m
	Height of cylinder	-	0.05	m

Assuming linear materials, the permanent magnets are made of Nd-Fe-B (N50) with the coercivity and relative permeability of 1050 KA/m and 1.38 T, respectively. The direction of MF has been taken along the  $z$ -axis corresponding with the axial direction of the permanent magnet ring. Similarly, the radial plane of the permanent

magnet ring is defined along the  $XY$  plane. Based on this ring-pair magnet model, a series of simulations and 3D finite element analysis of the magnet are conducted using the ANSYS v10.0 in this study.

Based on the requirements of the MRI system, the homogeneity and magnetic flux density (MFD) of the central imaging FOV are two important parameters that influence the performance of the magnet. Therefore, the model can be simplified to a mathematical formula as follows:

$$(B, U) = f(R_{in}, R_{out}, H, D), \quad (1)$$

where  $B$  and  $U$  are the MFD and homogeneity, respectively, as follows:

$$U = \frac{B_{max} - B_{min}}{B_{avg}}, \quad (2)$$

where  $B_{max}$ ,  $B_{min}$ , and  $B_{avg}$  are the maximum, minimum, and average MFDs of grid elements within the FOV volume used for the finite element method, respectively.

The ideal ring-pair magnet is magnetized uniformly in the radial direction, which is difficult to realize practically. Therefore, the magnet must be discretized along the radial direction. To generate a uniform central magnetic field, the magnets were divided into three even-numbered (4, 8, and 16) blocks (Fig. 3), with the black arrows representing the directions of magnetization.

The three models for the magnet were then simulated using ANSYS 10.0 simulator and the calculations were performed using the 3D finite element method. A solid 117-element type was utilized for the 3D static-MF analysis, which is an edge-based FEM, in ANSYS. Taking the 8 blocks model as an example, the magnet model was divided into approximately 30000 tetrahedron elements and 40000 nodes, as shown in Fig.4 (a). A finer and smaller mesh was used in the central imaging FOV, and the FOV contains 570 volume elements and 476 nodes (Fig. 4(b)). The MFD of each element is utilized to determine the homogeneity. The magnets were divided into 3081 volume elements and 2177 nodes that are larger as compared to those in the central imaging FOV. A slightly coarse grid meshing was utilized for the external part comprising air. A distance equivalent of five times the magnet size was defined as the air boundary condition, where the magnetic flux density was set to zero.

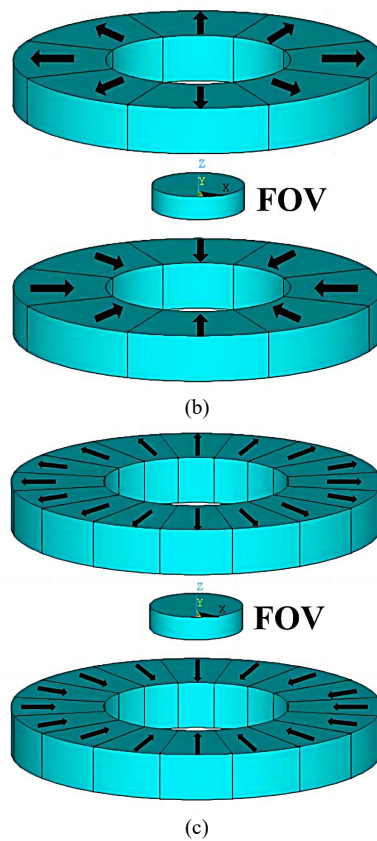
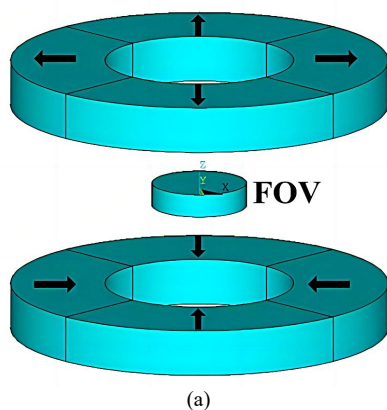


Fig. 3. Magnets discretized into different blocks along the radial direction for 4 (a), 8 (b), 16 (c) blocks.

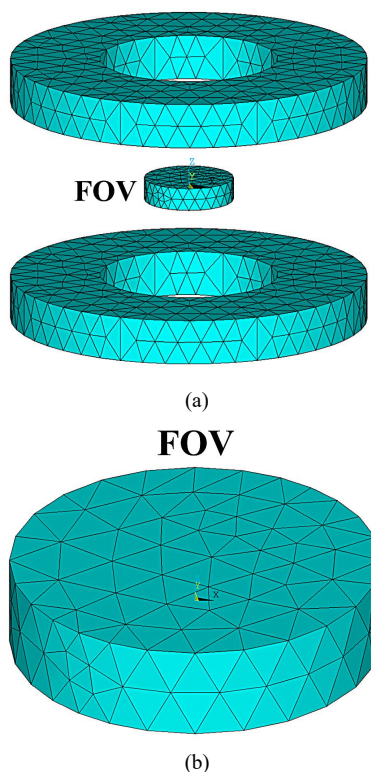


Fig. 4. The 3D meshing of the model for 8 blocks. (a) Magnet, (b) FOV.

Table II tabulates the results obtained from analyzing the magnetic field in the central imaging FOV. The analysis revealed that as the number of discrete blocks elevated, the average MFD in the FOV also increased. However, the homogeneity of the magnetic decreased indicating that the

magnetic field became increasingly uniform. It can be established that increasing the number of discrete blocks improves the magnetization and uniformity of MF. To achieve a uniform MF distribution in the FOV, a large number of discrete blocks is necessary. However, increasing the number of discrete blocks can pose challenges due to the increased processing and assembling requirements. Therefore, some trade-offs must be considered based on specific applications. The MF distribution in the central imaging FOV is illustrated in Fig. 5. It can be discerned that the MF distribution obtained from the three models essentially shows a similar pattern, with a stronger magnetic field in the middle and weaker field around the surrounding regions. The homogeneity of the MF distribution in the central imaging FOV can be enhanced by optimizing the relevant structural parameters, which will be conducted later.

TABLE II  
THE MF IN THE CENTRAL IMAGING FOV

Blocks	Average magnetic flux density, $B_{avg} / T$	Magnetic field homogeneity, $U / \text{ppm}, 10^{-6}$
4	0.1791	21012
8	0.1944	19708
16	0.1981	18481

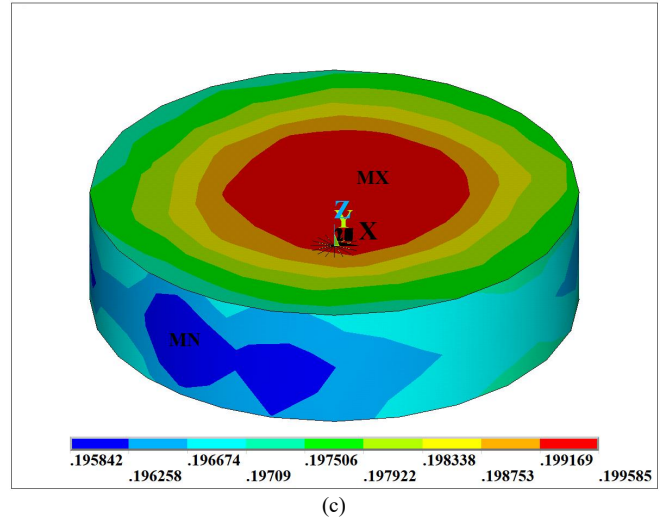
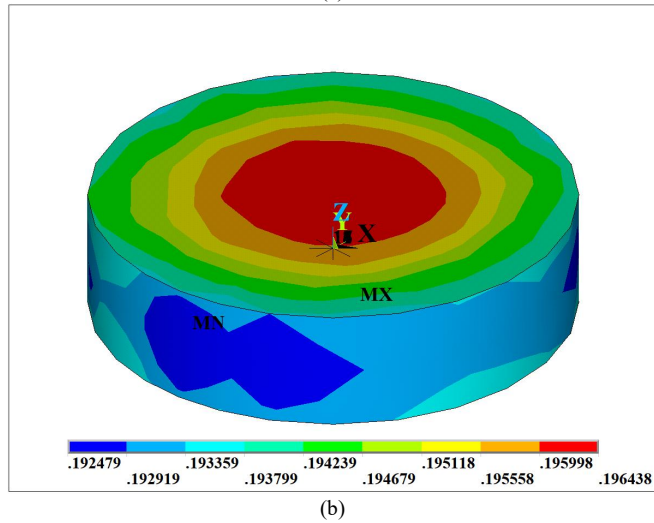
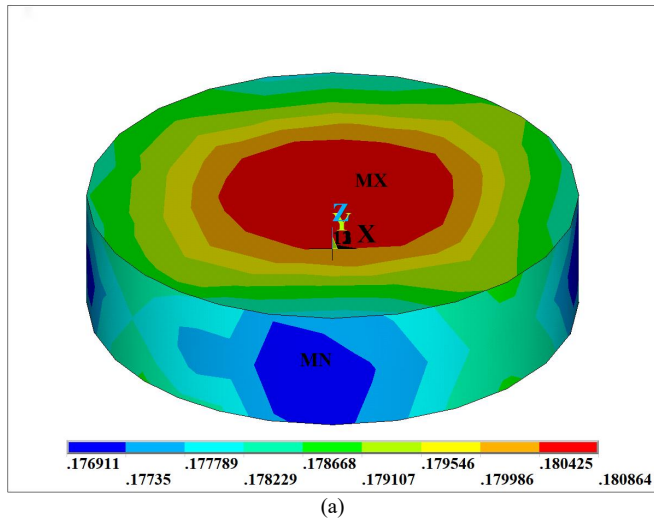


Fig. 5. Magnetic field distribution in the central imaging FOV for 4 (a), 8 (b), 16 (c) blocks.

### III. SENSITIVITY ANALYSIS OF THE PARAMETERS

#### A. Sobol Method

In the process of designing and optimizing the ring-pair magnet, certain structural parameters significantly affect the MF distribution in the FOV compared to others. When all structural parameters are optimized, the calculation can become time-consuming. In this context, SA can be used to quantitatively evaluate the effects of each parameter on the objective function and identify the key parameters. The SA approach considered in this study is based on the Sobol method, which is a well-established and widely adopted method based on variance. The model is defined as follows:

$$Y = f(x_1, x_2, \dots, x_n) \quad (3)$$

where  $x_1, x_2, \dots, x_n$  are input factors, while  $Y$  is output factor. The variance  $V$  of the output  $Y$  is decomposed as follows:

$$V(Y) = \sum_{i=1}^n V_i + \sum_{i < j \leq n} V_{ij} + \dots + V_{1,2,\dots,n} \quad (4)$$

Here,  $V_i = V[E(Y | x_i)]$ ,  $V_{ij} = V[E(Y | x_i, x_j)] - V_i - V_j$ , etc.. The Sobol method proposes two sensitivity indices (SIs) as follows:

$$S_i = \frac{V_i}{V(Y)}, \quad (5)$$

$$S_{Ti} = S_i + \sum_{j>i} S_{ij} + \dots + S_{1,\dots,n} = 1 - \frac{V_{-i}}{V(Y)}, \quad (6)$$

where  $S_i$  is the 1st-order SI of the  $i$ -th parameter and denotes the primary influence of  $x_i$  on output variance  $Y$ .  $S_{ij}$  denotes the interplay between  $i$ -th and  $j$ -th parameters and  $S_{Ti}$  represents the total SI, indicating the overall contribution of the  $i$ -th parameter to  $Y$ . This also involves the interaction between  $i$ -th input parameter and all other parameters. These parameters can be assigned to four groups according to the total sensitivity index ( $S_{Ti}$ ): very important ( $S_{Ti} > 0.8$ ), important ( $0.5 < S_{Ti} < 0.8$ ), not important ( $0.3 < S_{Ti} < 0.5$ ), and unrelated ( $S_{Ti} < 0.3$ ). The Monte Carlo approach was employed to produce randomly generated samples of input parameters, allowing for the estimation of the output expectation and variance, which can be used to compute the sensitivity indices via sensitivity analysis [14].

B. Sensitivity Analysis Results

The Monte Carlo method employed the aforementioned ring-pair magnet models to generate  $N = 4000$  random samples of input parameters. The resulting values for expectation and variance of the output were used to determine the sensitivity indices of the relevant structural parameters of the magnet. The detailed method can be seen elsewhere [15]. Three structural parameters, namely,  $H$ ,  $D$ , and  $R_{out}$ , were considered to analyze the MF distribution in the FOV. The size of the central imaging area can be determined by using  $R_{in}$  as a constant, and the sensitivity indices of  $R_{in}$  were not required, hence not analyzed in this work. Table III enlists the variation range of each structural parameter utilized for simulation purposes.

TABLE III  
RANGE OF THE PARAMETERS EMPLOYED FOR SIMULATION

Parameters	Range, m
$H$	[0.06, 0.15]
$D$	[0.3, 0.6]
$R_{out}$	[0.25, 0.5]
$R_{in}$	0.2 (constant value)

The 1st-order and total SIs for both  $U$  and  $B_{avg}$  were also determined using the Monte Carlo approach for the under-investigated three models. The results are displayed in Fig. 6. Specifically, from Figs. 6(a)-(b), it can be observed that in comparison with  $H$ ,  $U$  was significantly influenced by  $D$  and  $R_{out}$ . For the MF homogeneity  $U$ , the sensitivity order of the three investigated structural parameters is

$$R_{out} > D > H \quad (7)$$

Similarly, as demonstrated in Figs. 6 (c) and (d),  $B_{avg}$  of the FOV was sensitive to  $R_{out}$  as compared to the other parameters  $D$  and  $H$ . For the MFD  $B_{avg}$ , the sensitivity order of the 3 investigated structural parameters is

$$R_{out} > D > H \quad (8)$$

As can be seen, the trends of the sensitivity indices of different parameters obtained from the three models largely remained consistent. Since  $H$  remained insensitive, therefore, the value of  $H$  can be fixed to simplify the model and reduce the optimized search space. The parameters  $D$  and  $R_{out}$  were optimized in the subsequent optimization step.

IV. PARAMETER OPTIMIZATION AND RESULTS

The SA results in the preceding section revealed that  $D$  and  $R_{out}$  can significantly affect  $U$  and  $B_{avg}$  of the FOV, which need to be optimized, while  $H$  has a negligible impact on  $U$  and  $B_{avg}$ . Henceforth,  $H$  can be temporarily assigned a constant value of 0.1 m. The flow chart in Fig. 7 outlines the optimization process for the parameters. At the start of the process, the two parameters to be optimized were initialized, and the magnet model was generated in the ANSYS to determine the MF of the FOV. This study temporarily considered only a single optimization objective  $U$  of the FOV, with  $B_{avg} \geq 0.15$  T as a limiting condition. If the terminating condition is not fulfilled, the PSO algorithm will employ the updated parameters to re-evaluate the MF of the FOV.

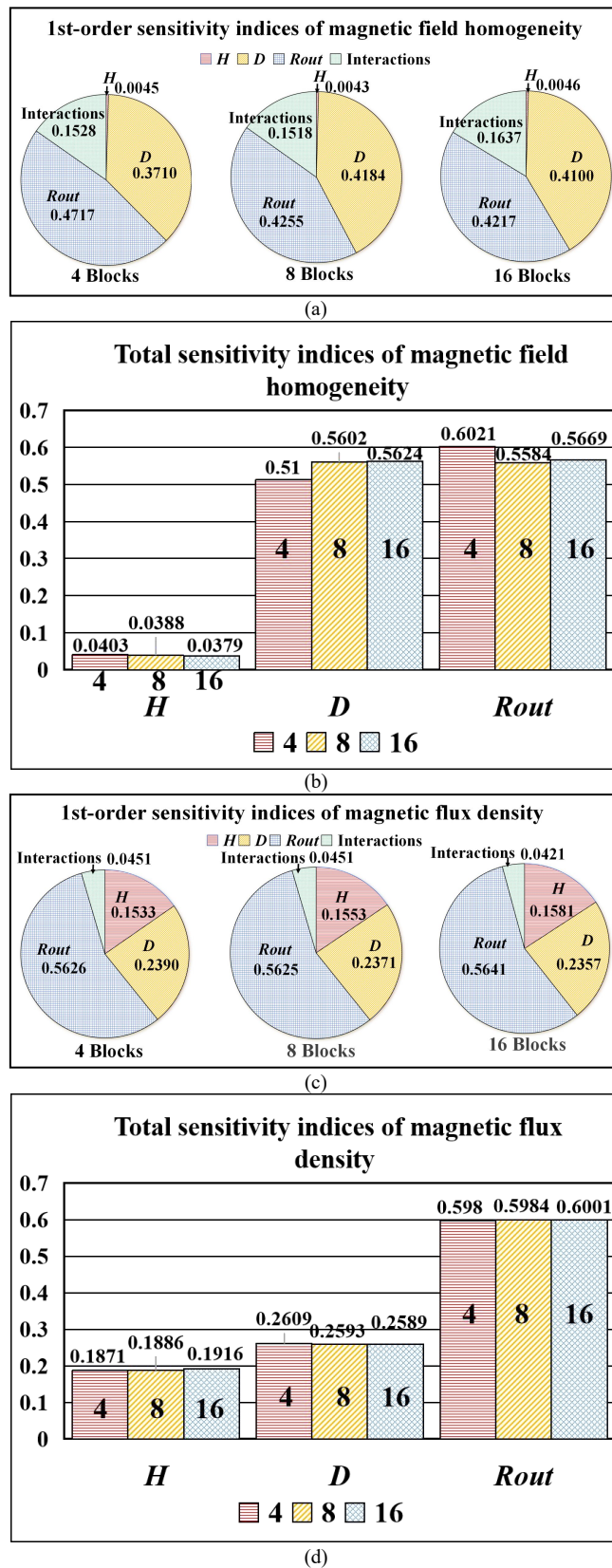


Fig. 6. SIs based on the ring-pair magnet models discretized into 4, 8, and 16 blocks. (a) 1st-order SIs of  $U$ , (b) Total SIs of  $U$ , (c) 1st-order SIs of  $B_{avg}$ , (d) Total SIs of  $B_{avg}$ .

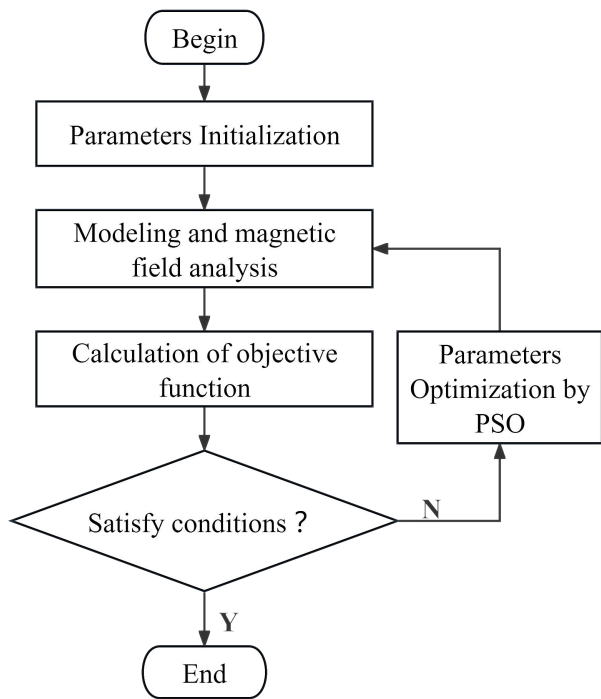


Fig. 7. Process of optimizing the parameters.

It has been observed that optimization of the electromagnetic fields can be complex due to non-linear complications and non-convex behavior with multi-pole points. This makes it challenging to identify the global optimum using traditional search algorithms. PSO is a progressive algorithm that has demonstrated excellent adaptability with a strong ability to perform global searches. Hence, this study employed the same algorithm to optimize the parameters.

A. PSO Algorithm

The flowchart for PSO algorithm is depicted in Fig. 8.

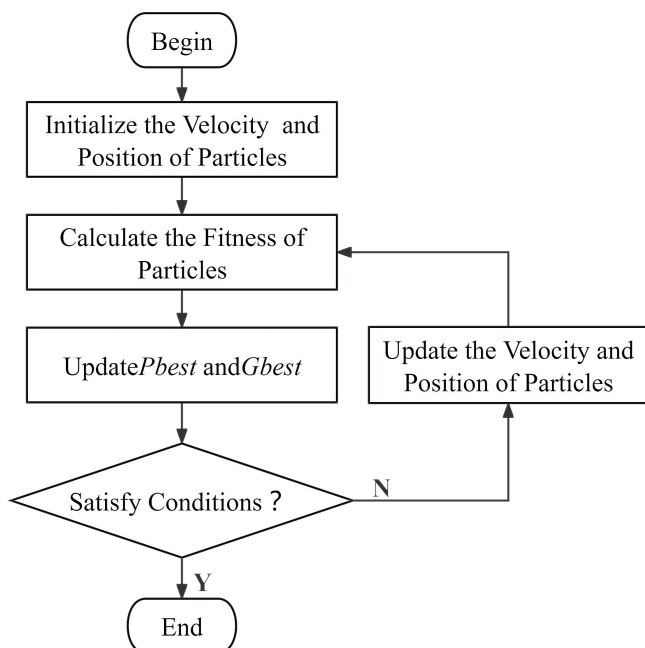


Fig. 8. Flow of the PSO algorithm.

In this algorithm, each solution is referred to as a particle. Initially, random particles are generated with initialized velocities and positions within the search space. Then, the particle's fitness values are determined, and the best previously known value of the particle position ( $Pbest$ ) is identified. Simultaneously, the optimal value of all the particles ( $Gbest$ ) from the swarm is determined. Through continuous iterations, the particles updated their directions and positions based on Equations (9) and (10), respectively, by exploring the solution space to identify the global optimal solution. The iterative optimization process persists until a specified number of iterations has been reached.

$$v_i^{k+1} = wv_i^k + C_1r_1(Pbest_i^k - x_i^k) + C_2r_2(Gbest^k - x_i^k), \quad (9)$$

$$x_i^{k+1} = x_i^k + v_i^{k+1} \quad (10)$$

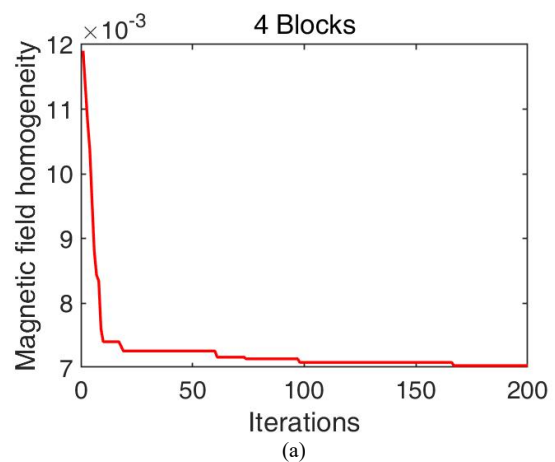
Where  $k$  denotes the iteration number,  $i$  signifies the  $i$ -th particle,  $x_i^k$  and  $v_i^k$  are the velocities of the  $i$ -th particle at the current position and the  $k$ -th iteration, respectively. Similarly,  $Pbest_i^k$  and  $Gbest^k$  are the optimized positions of the  $i$ -th particle according to its history and the overall swarm account, respectively. Furthermore,  $C_1$  and  $C_2$  represent positive constants fixed at the conventional value of 2 and  $w$  represents the inertial weight (range: 0.5-1). Moreover,  $r_1$  and  $r_2$  are random numbers (range: 0-1).

B. Optimization Results

The PSO method was utilized to optimize the structural parameters of  $D$  and  $R_{out}$  for the magnet models under investigation. We choose the magnetic field homogeneity  $U$  of the central imaging FOV as the target function and the PSO fitness criteria are formulated as follows:

$$\text{Minimize } U = \frac{B_{\max}(D, R_{out}) - B_{\min}(D, R_{out})}{B_{\text{avg}}(D, R_{out})}. \quad (11)$$

The count of particles was set to 30, and the relevant parameters of the PSO algorithm were defined. The optimization results were obtained after performing 200 iterations. The iterative convergence results of the three magnet model by PSO algorithm are depicted in Fig. 9.



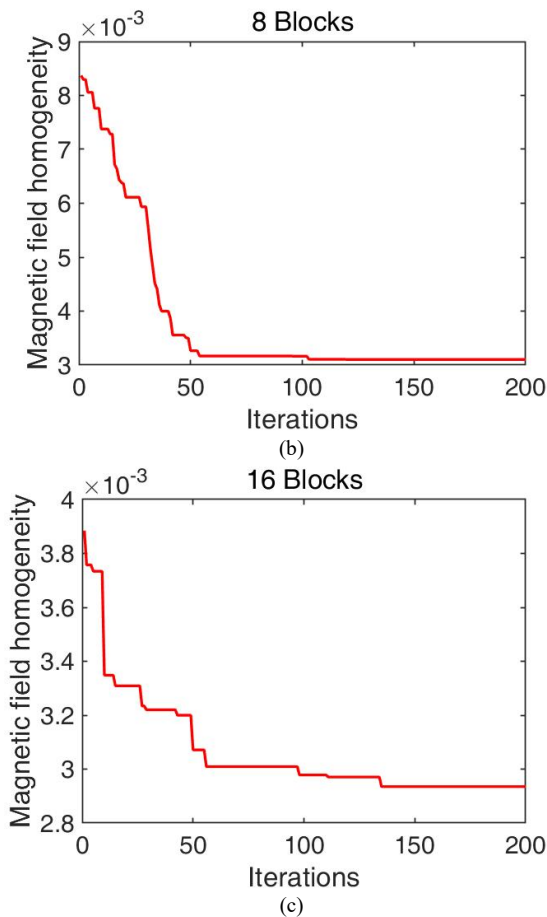


Fig. 9. Convergence effect of three magnet models for 4 (a), 8 (b), 16 (c) blocks.

Table IV presents the optimized values of structural parameters for three different magnet models. These results demonstrated the consistency in the optimized structural parameters across the three models. Specifically, the optimal value of  $D$  was found to be approximately 0.3895 m for the 16 Blocks model, while an optimized  $R_{out}$  of approximately 0.4758 m was observed for the 8 Blocks model of discretized ring-pair magnets.

TABLE IV  
OPTIMIZED STRUCTURAL PARAMETERS

Blocks	Parameters	Optimized value, m
4	$D$	0.3915
4	$R_{out}$	0.4711
8	$D$	0.3874
8	$R_{out}$	0.4758
16	$D$	0.3895
16	$R_{out}$	0.4781

The average MFD and homogeneity in the central imaging FOV were obtained and compared before and after optimization, as illustrated in Fig. 10. The initial magnetic model resulted in a magnetic flux density in the central imaging FOV of less than 0.2T, while the optimized magnet model achieved a higher density of greater than 0.2T, as evident from Fig. 10 (a). Similarly, from Fig. 10 (b), it was shown that the magnetic field homogeneity improved after optimization with values reducing to one-sixth of the initial value. The optimized magnet model, discretized into 16 blocks, resulted in the strongest and uniform magnetic field

distribution, with a minimum value of magnetic field homogeneity of 2935 ppm, corresponding to a flux density of 0.2527 T.

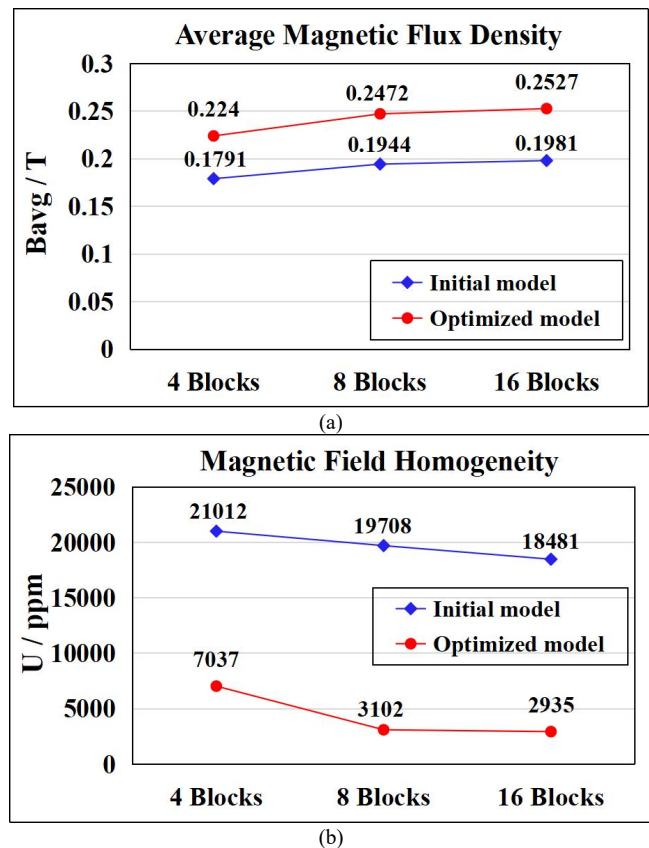


Fig. 10. Comparison between the magnetic fields in the central imaging FOV. (a) Average magnetic flux density, (b) Magnetic field homogeneity .

A detailed comparison of the MF distributions in the central imaging FOV of the optimized models is depicted in Fig. 11. Compared to Fig. 5, the optimized MF distributions in Fig. 11 appeared to be more uniform with significant enhancement in the MF observed in the central imaging FOV and the surrounding regions.

For the design of magnets, the MF distribution in the central FOV is the most important, which will directly affect the optimal image resolution. In the above work, the FOV was considered as a cylinder (diameter and height = 0.2 m and 0.05 m, respectively) in the middle of the 2 permanent magnets. To compare the magnetic field inside the central FOV for more details, we calculated different diameters of cylindrical FOV before and after optimization. All these cylinders share the origin of the coordinate system as their center, with diameters ranging from 8 cm to 20 cm. From these calculations, the minimum, maximum, and average MFDs were obtained. The statistical findings are presented in Fig. 12. The deviation within a small cylinder is smaller, indicating better uniformity compared to larger cylinders. Additionally, the deviations across various cylinders are consistently smaller for the three optimized magnet models than for the initial models, demonstrating that the optimized designs produce significantly more uniform MFs. Therefore, it can be established that the optimized magnet models can produce intense and highly uniform MFs in the central imaging FOV, leading to an improvement in the final imaging quality.

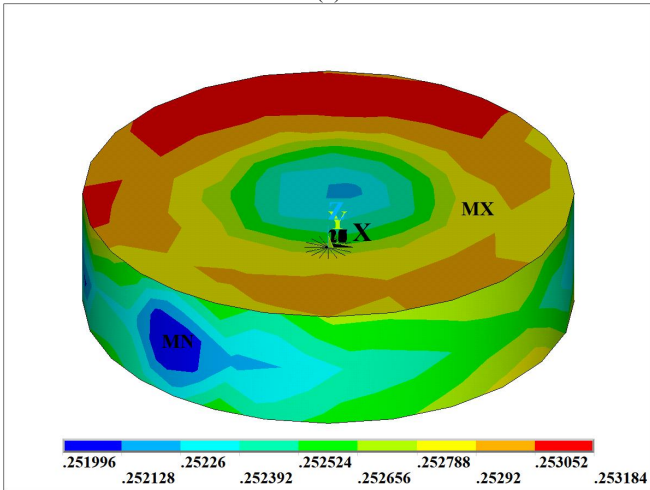
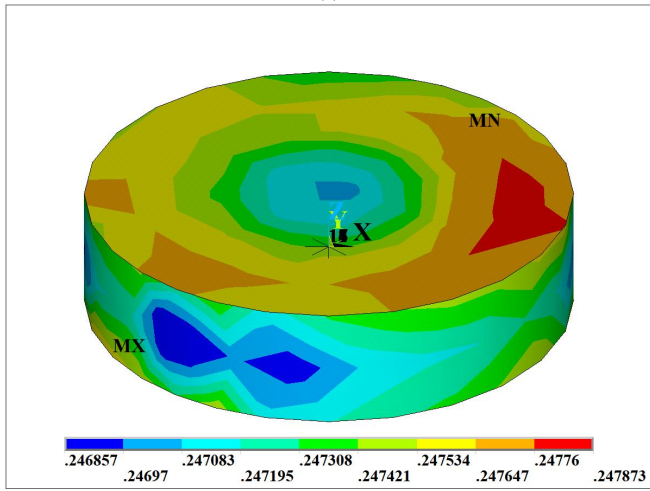
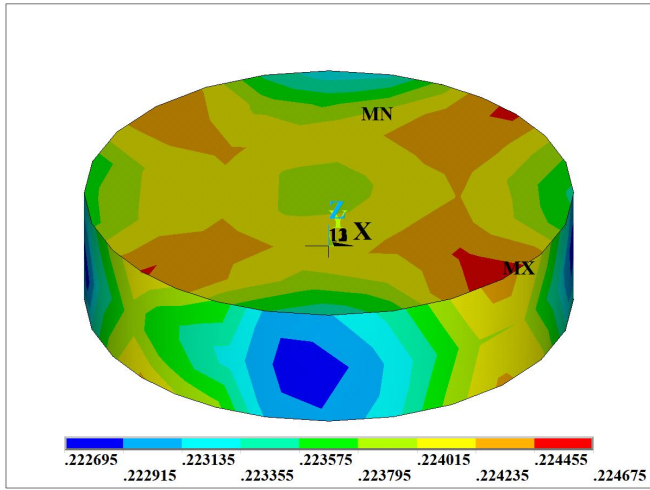
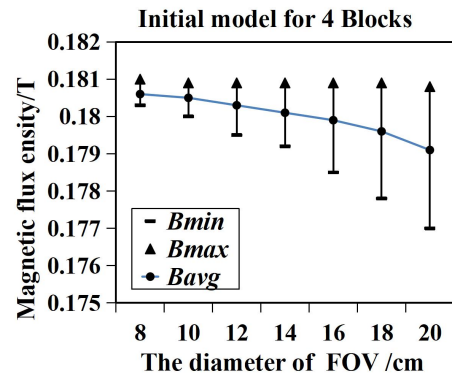
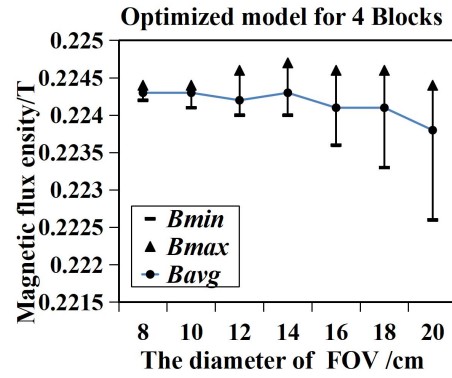


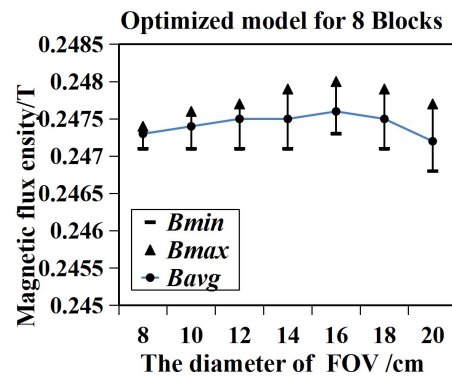
Fig. 11. Magnetic field distribution in the central FOV for 4 (a), 8 (b), and 16 (c) blocks.



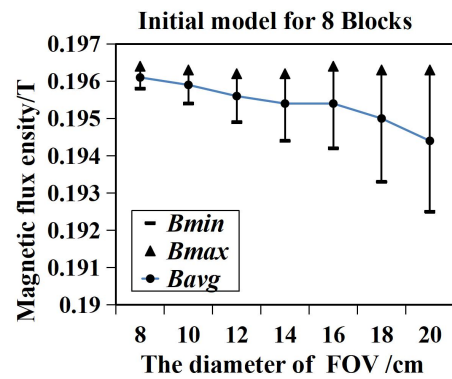
(a)



(b)



(c)



(d)

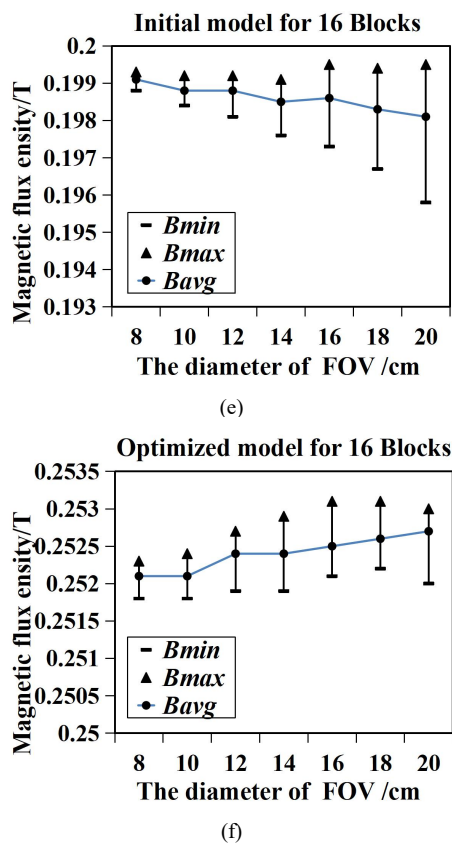


Fig. 12 The average MFD and deviation across various diameters of the central imaging FOV. (a) The initial models for 4 blocks, (b) The optimized model for 4 blocks, (c) The initial model for 8 blocks, (d) The optimized model for 8 blocks, (e) The initial model for 16 blocks, (f) The optimized model for 16 blocks.

## V. CONCLUSIONS AND DISCUSSIONS

This study focused on designing and simulating ring-pair permanent magnets for potential applications in portable MRI systems. Simulations were conducted using the ANSYS 10.0 software by employing the technique of finite element analysis. The magnet model was discretized into 4, 8, and 16 blocks along the radial direction, and electromagnetic fields were thoroughly analyzed. It was observed that increasing the number of discrete blocks led to higher average magnetic flux density in the FOV and improved magnetic field uniformity. The magnetic field approached the ideal uniform magnetization with an increasing number of discrete blocks. However, this also required significant utilization of computing resources. The Sobol method was used to quantitatively analyze the impact of certain structural parameters on the MF distribution within the FOV. The SA findings revealed that certain parameters, such as  $D$  and  $R_{out}$ , significantly affected the MF, and these were subsequently optimized. Similarly, it was found that  $H$  had a negligible effect on the magnetic field of the FOV, so a constant value was temporarily assigned to it in a bid to reduce the optimized search space. Upon optimizing the relevant structural parameters using the PSO algorithm, there was a significant improvement in the magnetic flux density and homogeneity, which could positively impact the final imaging quality in MRI systems.

The information provided in this work can lay the groundwork for designing and manufacturing actual magnets. However, in this study, the magnet model was only divided into sections along the radial direction. It would be beneficial

to explore segmenting the model along the axial direction to gain more insights into the parameters for analysis using the SA method. In the future, optimization methods are anticipated to be more comprehensive by simultaneously discretizing the magnet model along the axial and radial directions. Further collaboration with relevant companies will be sought to carry out manufacturing, testing, and verification of magnets.

## REFERENCES

- [1] G. Morrow, "Progress in MRI magnets," *IEEE Transactions on Applied Superconductivity*, vol. 10, No. 1, pp. 744-751, 2000.
- [2] A. Podol'skii, "Design procedure for permanent magnet assemblies with uniform magnetic fields for MRI devices", *IEEE Transactions on Magnetics*, vol. 36, No. 2, pp. 484-490, 2000.
- [3] H. S. Lopez, C. G. Salmon, C. C. Mirabal, H. Saint-Jalmes, "Designing an efficient resistive magnet for magnetic resonance imaging," *IEEE Transactions on Magnetics*, vol. 40, No.5, pp. 3378-3381, 2004.
- [4] J. H. Bae, K. D. Sim, R. K. Ko, Y. K. Kwon, K. S. Ryu, Y. S. Jo, "The fabrication of superconducting magnet for MRI", *Physica C Superconductivity*, vol. 372, No.2, pp. 1342-1345, 2002.
- [5] T. Kimura, Y. Geya, Y. Terada, K. Kose, T. Haishi, H. Gemma, Y. Sekozawa, "Development of a mobile magnetic resonance imaging system for outdoor tree measurements," *Review of Scientific Instruments*, vol. 82, No.5, pp. 053704, 2011.
- [6] M. Nakagomi, M. Kajiwara, J. Matsuzaki, K. Tanabe, S. Hoshiai, Y. Okamoto, Y. Terada, "Development of a small car-mounted magnetic resonance imaging system for human elbows using a 0.2 T permanent magnet," *Journal of Magnetic Resonance*, vol. 304, pp. 1-6, 2019.
- [7] C. Z. Cooley, M. W. Haskell, S. F. Cauley, C. Sappo, C. D. Lapiere, C. G. Ha, J. P. Stockmann, L. L. Wald, "Design of Sparse Halbach Magnet Arrays for Portable MRI Using a Genetic Algorithm," *IEEE Transactions on Magnetics*, vol. 54, No. 1, pp. 1-12, 2018.
- [8] B. Blümich, "Low-field and benchtop NMR," *Journal of Magnetic Resonance*, vol. 306, pp. 27-35, 2019.
- [9] C. Hugon, M. A. Pedro, G. Aubert, D. Sakellariou, Design, "Fabrication and Application of a Low-Cost Homogeneous Portable Permanent Magnet for NMR and MRI," *Comptes Rendus Chimie*, vol. 13, No. 4, pp. 388-393, 2010.
- [10] C. Hugon, D. A. Francesca, G. Aubert, D. Sakellariou, "Design of arbitrarily homogeneous permanent magnet systems for NMR and MRI: Theory and experimental developments of a simple portable magnet," *Journal of Magnetic Resonance*, vol. 205, No. 1, pp. 75-85, 2010.
- [11] Z. H. Ren, W. Mu, S. Y. Huang, "Design and Optimization of a Ring-Pair Permanent Magnet Array for Head Imaging in a Low-Field Portable MRI System," *IEEE Transactions on Magnetics*, vol. 55, No. 1, pp. 1-8, 2019.
- [12] Z. H. Ren, J. Gong, S. Y. Huang, "An Irregular-Shaped Inward-Outward Ring-Pair Magnet Array With a Monotonic Field Gradient for 2D Head Imaging in Low-Field Portable MRI," *IEEE Access*, vol. 7, pp. 48715-48724, 2019.
- [13] Z. H. Ren, "Advance Low-field Portable Magnetic Resonance Imaging (MRI) by Applying Electromagnetics Concepts," Ph.D. dissertation, Engineering Product Development, Singapore University of Technology and Design, Singapore, 2020.
- [14] A. Saltelli, "Making best use of model evaluations to compute sensitivity indices," *Computer Physics Communications*, vol. 145, No.2, pp. 280-297, 2002.
- [15] Y. Y. Cheng, W. He, L. Xia, F. Liu, "Design of shimming rings for small-sized permanent MRI magnet using sensitivity-analysis-based particle swarm optimization algorithm," *Journal of Medical and Biological Engineering*, vol. 35, No. 4, pp. 448-454, 2015.

Yi-Yuan Cheng, born in Henan, China, in 1985, obtained her Bachelor of Engineering (B.E.) degree in Biomedical Engineering from South-Central University for Nationalities, Wuhan, China, in 2008. She completed her Ph.D. in Biomedical Engineering at Zhejiang University, Hangzhou, China, in 2015. She currently serves as an Associate Professor in the Department of Intelligent Manufacturing and Electrical Engineering at Nanyang Normal University, Nanyang, China. Her research interests primarily focus on artificial intelligence, magnet design and optimization, MRI and related fields.

Ming-Yang Su, born in Henan, China, in 1984, earned his Bachelor of Engineering (B.E.) degree in 2006 and his Master's degree in 2010 from Qingdao University of Science and Technology, Qingdao, China. He is

currently a lecturer at Henan Polytechnic Institute, Nanyang, China. His primary research focuses on materials science.

Yi-Ding Huang, born in Henan, China, in 1974, obtained her Bachelor of Engineering (B.E.) degree from PLA Information Engineering University, Zhengzhou, China, in 2002, and her Master's degree from Jiangnan University, Wuxi, China. She is currently serving as an associate professor in the Department of Intelligent Manufacturing and Electrical Engineering at Nanyang Normal University, Nanyang, China. Her primary research interests include the integrated design and application of mechatronics.

Wei Liu, born in Henan, China, in 1983, earned his Bachelor of Engineering (B.E.) degree in 2006 and Master's degree in 2009 from Zhengzhou University, Zhengzhou, China. He completed his Ph.D. in 2012 at the Institute of Automation, Chinese Academy of Sciences, Beijing, China. Currently, he holds a professorship in the Department of Intelligent Manufacturing and Electrical Engineering at Nanyang Normal University, Nanyang, China. His primary research interests include machine vision, artificial intelligence, and related fields.